



HAL
open science

Non-reciprocal Pauli Spin Blockade in a Silicon Double Quantum Dot

Theodor Lundberg, David J. Ibberson, Jing Li, Louis Hutin, José C. Abadillo-Uriel, Michele Filippone, Benoit Bertrand, Andreas Nunnenkamp, Chang-Min Lee, Nadia Stelmashenko, et al.

► To cite this version:

Theodor Lundberg, David J. Ibberson, Jing Li, Louis Hutin, José C. Abadillo-Uriel, et al.. Non-reciprocal Pauli Spin Blockade in a Silicon Double Quantum Dot. npj Quantum Information, 2024, 10 (1), pp.28. 10.1038/s41534-024-00820-1 . hal-03413253

HAL Id: hal-03413253

<https://hal.science/hal-03413253v1>

Submitted on 21 Aug 2024

HAL is a multi-disciplinary open access archive for the deposit and dissemination of scientific research documents, whether they are published or not. The documents may come from teaching and research institutions in France or abroad, or from public or private research centers.

L'archive ouverte pluridisciplinaire **HAL**, est destinée au dépôt et à la diffusion de documents scientifiques de niveau recherche, publiés ou non, émanant des établissements d'enseignement et de recherche français ou étrangers, des laboratoires publics ou privés.



Distributed under a Creative Commons Attribution 4.0 International License

<https://doi.org/10.1038/s41534-024-00820-1>

Non-symmetric Pauli spin blockade in a silicon double quantum dot

Check for updates

Theodor Lundberg^{1,2}, David J. Ibberson^{2,3,4,9}, Jing Li^{5,6}, Louis Hutin⁶, José C. Abadillo-Uriel⁵, Michele Filippone⁵, Benoit Bertrand⁶, Andreas Nunnenkamp⁷, Chang-Min Lee⁸, Nadia Stelmashenko⁸, Jason W. A. Robinson⁸, Maud Vinet⁶, Lisa Ibberson², Yann-Michel Niquet⁵ & M. Fernando Gonzalez-Zalba⁹ ✉

Spin qubits in gate-defined silicon quantum dots are receiving increased attention thanks to their potential for large-scale quantum computing. Readout of such spin qubits is done most accurately and scalably via Pauli spin blockade (PSB), however, various mechanisms may lift PSB and complicate readout. In this work, we present an experimental study of PSB in a multi-electron low-symmetry double quantum dot (DQD) in silicon nanowires. We report on the observation of non-symmetric PSB, manifesting as blockaded tunneling when the spin is projected to one QD of the pair but as allowed tunneling when the projection is done into the other. By analyzing the interaction of the DQD with a readout resonator, we find that PSB lifting is caused by a large coupling between the different electron spin manifolds of 7.90 μeV and that tunneling is incoherent. Further, magnetospectroscopy of the DQD in 16 charge configurations, enables reconstructing the energy spectrum of the DQD and reveals the lifting mechanism is energy-level selective. Our results indicate enhanced spin-orbit coupling which may enable all-electrical qubit control of electron spins in silicon nanowires.

Spin qubits in gate-defined silicon quantum dots (QDs) have emerged as a promising platform for implementing large-scale quantum computation owing to their long coherence times, compact size and ability to be operated at relatively high temperatures of 1–4 K^{1–6}. Moreover, silicon spin qubits can be fabricated using industrial semiconductor manufacturing techniques, thereby presenting a path to high-yield large-scale device fabrication in which control electronics may also be integrated on-chip^{7–11}. With the increasing emphasis on scalability, it is becoming attractive to pursue methods of spin qubit control^{12–15} and readout^{16–19} that could simplify the processor architecture by avoiding additional on-chip components and layout constraints such as charge reservoirs.

In terms of readout, silicon spin qubits are measured using spin-to-charge conversion, a process that translates the spin degree of freedom to a selective movement of charge. Such conversion is typically performed via spin-selective tunneling to a reservoir²⁰ or via Pauli spin blockade (PSB) between spins in two QDs²¹. In both cases, the movement of charge can be

detected using sensitive charge sensors, such as the single-electron transistor²² or the single-electron box²³. However, PSB offers the substantial advantage that it can be detected dispersively, using external resonant circuits, thus alleviating the need for electrometers and charge reservoirs adjacent to the qubit, leading to a simplified processor architecture^{24,25}. Moreover, PSB has been shown to provide high-fidelity readout, even at low magnetic fields and elevated temperatures^{5,26–28}.

PSB works under the exclusion principle in which two fermionic particles cannot possess all the same quantum numbers. In practice, the combined spin state of two separated electrons (or holes) in two QDs is projected into that of a single QD whose ground state is the joint singlet. If the initial state was a singlet, tunneling occurs, if it was a triplet, tunneling is forbidden. Such process is expected to be symmetric, i.e., independent of QD used for the projection. PSB, however, may be lifted thus compromising readout. Lifting of PSB may occur partially, due to fast relaxation of the unpolarized T^0 state resulting in parity-only readout²⁹ or fully, due to direct

¹Cavendish Laboratory, University of Cambridge, J.J. Thomson Avenue, Cambridge CB3 0HE, UK. ²Hitachi Cambridge Laboratory, J.J. Thomson Avenue, Cambridge CB3 0HE, UK. ³Quantum Engineering Technology Labs, University of Bristol, Tyndall Avenue, Bristol BS8 1FD, UK. ⁴Quantum Engineering Centre for Doctoral Training, University of Bristol, Tyndall Avenue, Bristol BS8 1FD, UK. ⁵Université Grenoble Alpes, CEA, IRIG, MEM/L_Sim, 38000 Grenoble, France. ⁶Université Grenoble Alpes, CEA, LETI, 38000 Grenoble, France. ⁷Faculty of Physics, University of Vienna, Boltzmannngasse 5, 1090 Vienna, Austria. ⁸Department of Materials Science and Metallurgy, University of Cambridge, 27 Charles Babbage Road, Cambridge CB3 0FS, UK. ⁹Present address: Quantum Motion, 9 Sterling Way, London N7 9HJ, UK. ✉e-mail: fernando@quantummotion.tech

tunneling between triplet states²⁴, due to hyperfine or spin-orbit interactions³⁰ or due to fast tunneling to low-energy high-spin states, such as a spin quintet, which may result from small valley-orbit splittings and generally dense QD energy spectra^{31,32}. Generally, theory predicts that fast relaxation processes happening at rates similar or faster than the readout probe frequency lift dispersively-detected PSB³³. More recently, it has been predicted that in systems with strong spin-orbit coupling, PSB may only occur near magnetic field orientations that align with the eigenvectors of the combined DQD g -tensor³⁴.

In this Letter, we report on the observation of non-symmetric PSB in silicon QDs, manifesting as PSB when the spin is projected to one QD of the pair but as lifted PSB when the projection is done into the other QD. Particularly, we observe the phenomenon in a multi-electron silicon DQD formed using a split-gate nanowire transistor. Multi-electron QDs are receiving close attention due to their capability to better screen potential disorder and facilitate dot-to-dot couplings which will be advantageous for future scaling^{35,36}. By studying spin tunneling between the QDs across 16 different charge configurations using dispersive readout, we find (i) that PSB can still occur despite the low-symmetry of the QDs, although PSB lifting is highly prevalent and (ii) that PSB may be non-symmetric, i.e., for a given charge configuration (N, M) , PSB occurs by projecting the state either to the $(N + 1, M - 1)$ or $(N - 1, M + 1)$ states but not both. We further analyse the response of the readout resonator using input-output theory, and find that (i) PSB lifting is caused by a large coupling between the different electron spin manifolds of up to $7.90 \mu\text{eV}$ and (ii) that tunneling between spin states does not preserve phase.

Results

Non-symmetric Pauli spin blockade

Figure 1a shows the split-gate nanowire field-effect transistor used in this work. To perform gate-based sensing, we wirebond gate G_{T1} , which overlaps the channel $7 \pm 3 \text{ nm}$ more than G_{B1} , to a superconducting NbN spiral inductor on a separate chip, thus forming a LC resonant circuit with resonance frequency $f_0(B = 0) = 1.88 \text{ GHz}$ at zero magnetic field. For further details about the transistor, inductor, and setup, see “Description of device and measurement setup” and ref. 37. A DQD constituted by a pair of low-symmetry QDs is formed in the upper corners of the nanowire channel when positive voltages, applied to G_{B1} and G_{T1} , attract electrons from the source and drain reservoirs. The QDs appear in a parallel configuration with respect to the reservoirs (see “Simulation of device electron density” for simulations of the three-dimensional electron density in the device). The number of electrons accumulated in the DQD is set by the gate voltages V_{B1} and V_{T1} , whereas changes in the DQD electron occupancy are detected dispersively by probing the resonator via the transmission line MW_{in} at frequency f close to f_0 while monitoring the phase shift of the reflected signal ϕ . We observe phase changes at the charge degeneracy regions due to the cyclical interdot charge transitions (ICT) or dot-to-reservoir charge tunneling events driven by the microwave excitation^{33,37}, see Fig. 1b and “Zoomed-in ICT charge stability diagrams” for zoom-ins on the ICT regions. We determine the electron occupancy (N_{T1}, N_{B1}) indicated in Fig. 1b using one QD as a charge sensor for the other QD³² (see Appendix D in ref. 37 for the charge population data of the device also used in this work). We can control the charge occupation down to the last electron in both QDs. ICTs are not visible for electron populations smaller than those presented on this plot as a result of insufficient wavefunction overlap for tunneling to occur on the timescale of the resonator period³⁸. While this Article shall eventually investigate all 16 ICTs visible in Fig. 1b, we first consider the pair of neighboring ICTs between the $(7,8)$, $(6,9)$ and $(5,10)$ charge states highlighted by the dotted boxes in Fig. 1b which share a common charge state, the $(6,9)$. Given that in silicon QDs without spatial symmetries the first two full electronic shells occur for charges states $N_{T1(B1)} = 4$ and 8 , the three states may be considered equivalent to $(3,0)$, $(2,1)$ and $(1,2)$, for simplicity. We represent them in the single-particle diagrams of Fig. 2a, b and as shown in “Energy-level diagrams for all 16 ICTs at $B = 0 \text{ T}$ and $B = 0.4 \text{ T}$ ”.

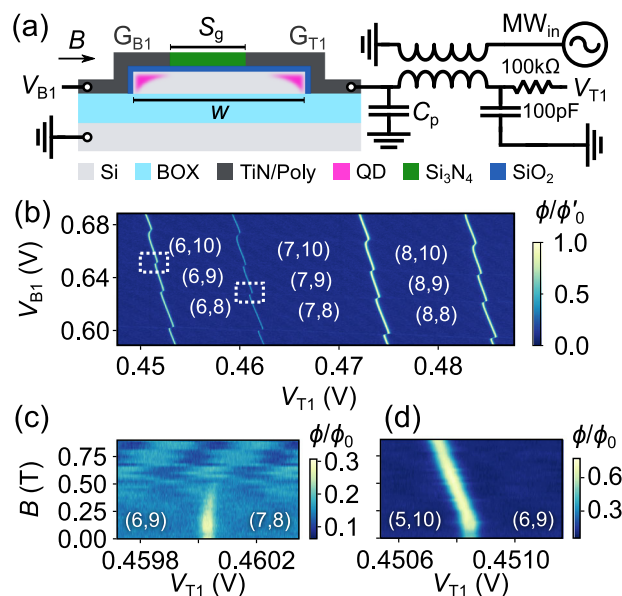


Fig. 1 | Non-symmetric PSB in a pair of neighbouring ICTs. **a** Sketch of the device cross-section perpendicular to the direction of the nanowire illustrating the device architecture and the formation of a DQD in the upper channel corners. The LC resonant circuit, comprised of the DQD connected via gate G_{T1} to a superconducting NbN planar spiral inductor, is inductively coupled to a microstrip waveguide to enable dispersive readout. **b** Charge stability diagram of the DQD recorded using gate-based dispersive sensing while sweeping the electrostatic potentials of G_{T1} and G_{B1} . The numbers in parentheses indicate the electron occupancy of the DQD and the dotted rectangles highlight the ICTs studied in (c) and (d) as well as in Fig. 2. **c, d** Measurement of the relative phase shift of the $(6,9)$ – $(7,8)$ and $(5,10)$ – $(6,9)$ ICTs as a function of magnetic field B showing non-symmetric PSB.

To probe the excited state spin spectrum of the DQD and in particular of the $(6,9)$ – $(7,8)$ and $(5,10)$ – $(6,9)$ ICTs, we measure V_{T1} line traces that intersect the center of each ICT while increasing B from 0 to 0.9 T ^{31,32,39}. The magnetic field is applied in-plane with the device and perpendicular to the nanowire direction, and the probe frequency f is continuously adjusted to account for the changing kinetic inductance of the NbN inductor. The resulting dispersive magnetospectroscopy measurements shown in Fig. 1c, d plot the relative phase shift ϕ/ϕ_0 , where ϕ_0 is the largest phase shift measured among the 16 ICTs in Fig. 1b. In the case of the $(6,9)$ – $(7,8)$ transition (Fig. 1c), the signal starts to vanish asymmetrically as the magnetic field is increased, which is the signature of dispersively-detected PSB^{19,24,31–33,39–43}. More particularly, at low magnetic fields, the system is free to cyclically tunnel between two states with the same spin number (high ϕ/ϕ_0) due to the oscillatory resonator drive. However, as the magnetic field is increased, a higher spin state becomes the ground state of the system at the aforementioned transition point. If the new higher spin state does not couple with the lower spin states, the system gets blocked in the higher spin state and the signal disappears since no cyclic tunneling can occur. The slope at which the signal in Fig. 1c vanishes, which tracks the crossing point between the two spin manifolds involved, enables extracting the interdot gate lever arm, $\alpha = 0.660$, assuming an average electron g -factor of 2 . Because of the shared charge state between the transitions $(6,9)$ – $(7,8)$ and $(5,10)$ – $(6,9)$, one might expect the $(5,10)$ – $(6,9)$ ICT to also show PSB^{40,44} since this represents the symmetric projection of the spin, but now on to the opposite QD. However, in Fig. 1d, instead of asymmetrically vanishing, the signal of this ICT persists and remains constant beyond $B = 0.16 \text{ T}$ tracking the point at which the two spin manifolds should cross. Such result implies cycling tunneling occurs between two states with different spin number, i.e., PSB lifting. This striking result in which PSB is non-symmetric, is the focus of the manuscript. We note the slope of the signal in Fig. 1d above $B = 0.16 \text{ T}$

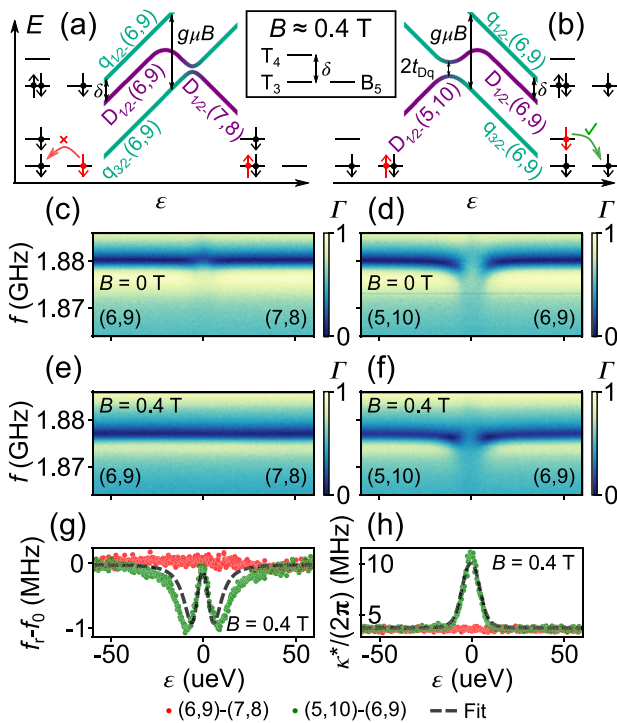


Fig. 2 | Level-selective PSB and decoherence. **a, b** Illustrative single-particle and DQD energy levels for the (5,10), (6,9) and (7,8) charge states at $B \approx 0.4$ T as a function of detuning ϵ . The red electrons and green (red) arrows indicate (the lack of) spin flip tunneling between the doublet $D_{1/2}$ and quadruplet $q_{3/2}$ ground states. For simplicity, the single-particle energy levels omit the two (four) lowest-lying energy levels of QD_{T1} (QD_{B1}). **c–f** Reflection coefficient of the resonator Γ as a function of f and ϵ for the (6,9)–(7,8) and (5,10)–(6,9) ICTs at $B = 0$ T and $B = 0.4$ T. **g, h** Resonance frequency and effective linewidth as a function of ϵ for ICTs (6,9)–(7,8) [red] and (5,10)–(6,9) [green] at $B = 0.4$ T determined by Lorentzian fits to the data in (e) and (f).

implies in this case an interdot lever arm, $\alpha = 0.789$ (see Fig. 1d and “Maximum phase shift of (5,10)–(6,9) ICT vs magnetic field”).

To facilitate the understanding of the non-symmetric presence of PSB in Fig. 1c, d, we focus on the three outermost electrons in the DQD and sketch the single- and multi-particle energy levels for these electrons. In the (5,10), (6,9), and (7,8) charge states, the three outermost electrons are distributed between the T_3 , T_4 , and B_5 energy levels shown in the inset of Fig. 2a, b, where T_i (B_j) refers to the i^{th} (j^{th}) energy level of QD_{T1} (QD_{B1}). By populating the single-particle energy levels with the number of electrons corresponding to the charge state, we observe that the electrons in the DQD may form doublets D, with one unpaired electron and a spin angular momentum $S = 1/2$, or quadruplets q with three unpaired electrons and $S = 3/2$. Here, we assume that the exchange energy is smaller than the single-particle energy level spacing⁴⁵. At $B = 0$ T, the ground state $D(6,9)$ is separated from the first excited state $q(6,9)$ by $\delta = 18.65$ μeV (see Appendices IV E and IV H for extraction of δ and energy spectra at $B = 0$ T). However, as B is increased, the states Zeeman split according to $E_Z = m_s g \mu_B B$, where m_s is the spin angular-momentum projection onto the B -axis, g is the electron g -factor and μ_B is the Bohr magneton, thus causing the lowest energy quadruplet $q_{3/2}$ to become the (6,9) ground state when $g \mu_B B > \delta$. This situation is sketched in Figs. 2a, b, which show the energy levels of the DQD as a function of detuning ϵ at $B \approx 0.4$ T. From these energy levels, one would expect the ground state electron transitions $q_{3/2}-(6,9)$ - $D_{1/2}$ -(7,8) and $q_{3/2}-(6,9)$ - $D_{1/2}$ -(5,10), highlighted by the red electrons and arrows in Fig. 2a, b respectively, to be spin-blocked due to the Pauli exclusion principle. However, recalling Fig. 1, PSB is only present for the (6,9)–(7,8) transition involving levels T_3 and B_5 , and not for the (5,10)–(6,9) transition, which involves levels T_4 and B_5 . This hints at a level-selective process that allows spin-flip tunneling as the

explanation for the signal generated at the $D_{1/2}$ -(5,10)- $q_{3/2}$ -(6,9)-intersection as a function of B . We further note that the allowed spin-independent transition, $D(5,10)$ - $D(6,9)$, involves the same single-particle levels as the spin-blocked transition in Fig. 2c, reinforcing the idea that a change in spin number is a necessary condition for the disappearance of the signal.

Pauli spin blockade lifting mechanism

We further investigate the two ICTs by studying the reflected spectrum of the resonator while changing detuning $\epsilon = e\alpha(V_{T1} - V_{T1}^0)$, where V_{T1}^0 is the central position of the measured ICT, at both $B = 0$ T and $B = 0.4$ T [see Fig. 2c–f]⁴⁶. To describe the coupled resonator-DQD system, we use the circuit quantum electrodynamics framework⁴⁷. Due to the effective coherent DQD-resonator coupling given by $g_{\text{eff}ij}/(2\pi) = g_0/(2\pi)\langle i|\hat{n}|j\rangle$ between states i and j , where $\langle i|\hat{n}|j\rangle$ is the coupling matrix element, and \hat{n} is the charge number operator, we observe changes in the resonance frequency f_r and the effective linewidth κ^* of the resonator according to^{37,48,49}

$$f_r = f_0 - \frac{1}{2\pi} \frac{g_{\text{eff}ij}^2 \Delta_{ij}}{\Delta_{ij}^2 + \gamma_{ij}^2/4} \quad (1)$$

$$\kappa^*/(2\pi) = \kappa/(2\pi) + \frac{1}{2\pi} \frac{g_{\text{eff}ij}^2 \gamma_{ij}}{\Delta_{ij}^2 + \gamma_{ij}^2/4} \quad (2)$$

where t_{ij} is the DQD tunnel coupling, $\Omega_{ij} = \sqrt{\epsilon^2 + 4t_{ij}^2}$ is the energy difference between participating states, $\Delta_{ij} = \Omega_{ij}/\hbar - 2\pi f_0$, κ is the bare resonator linewidth, and γ_{ij} is the DQD decoherence rate. Here, we have defined $g_0/(2\pi) = \alpha f_0 \sqrt{Z_r/2R_Q}$ in which we assume α is constant for a given charge configuration, R_Q is the resistance quantum, and Z_r is the resonator impedance. By applying these equations to the measurements in Fig. 2c–f, we deduce important information about the DQD.

First, we analyze the resonator response at $B = 0$ T in Fig. 2c. The data reveals an upwards shift of f_r around $\epsilon = 0$ thus indicating $g_{\text{eff}DD} > 0$ and $\Delta_{DD} < 0$, which implies $0 < 2t_{DD} < \hbar f_0 = 7.8$ μeV between the states $D(6,9)$ and $D(7,8)$. Despite being in the resonant regime at some ϵ where $\Omega_{DD} = \hbar f_0$, we do not observe characteristic vacuum Rabi-mode-splitting due to the large decoherence rate, γ_{DD} , of this charge transition indicated by the increased κ^* around $\epsilon = 0$ (see “Resonator response for ICTs (6,9)–(7,8) and (5,10)–(6,9) at $B = 0$ T”). By similar inspection of now Fig. 2d, we find a downwards shift of f_r around $\epsilon = 0$ indicating that $g_{\text{eff}DD'} > 0$ and $\Delta_{DD'} > 0$, implying $2t_{DD'} > \hbar f_0 = 7.8$ μeV between the states $D(5,10)$ and $D(6,9)$.

To understand the origin of non-symmetric PSB, we repeat the analysis but now at $B = 0.4$ T as shown in Fig. 2e and f. We further fit each ϵ trace of the response to a Lorentzian with center frequency f_r and linewidth $\kappa^*/(2\pi)$ (see “Description of fitting procedures” for description of fitting procedure). As can be seen from the red (6,9)–(7,8) data in Fig. 2g, h, there are no changes to f_r or κ^* around $\epsilon = 0$, thus indicating that the coupling matrix element $\langle q_{3/2}-(6,9)|\hat{n}|D_{1/2}-(7,8)\rangle \rightarrow 0$ and hence $t_{Dq}(6,9)(7,8) \rightarrow 0$. This conclusion is in line with the lack of phase response at $B \geq 0.4$ T due to PSB seen in Fig. 1c. However, for the (5,10)–(6,9) transition, represented by the green data in Fig. 2g, h, the shift in f_r and increase in κ^* around $\epsilon = 0$ indicates $g_{\text{eff}Dq} > 0$ for states $D_{1/2}$ -(5,10) and $q_{3/2}$ -(6,9). The observation that f_r first decreases symmetrically with decreasing $|\epsilon|$ indicates $\Delta_{Dq} > 0$ whereas the subsequent increase to $f_r \approx f_0$ at $\epsilon = 0$ indicates $\Delta_{Dq} \rightarrow 0$ when $\epsilon \rightarrow 0$. This implies a $D_{1/2}$ -(5,10)- $q_{3/2}$ -(6,9) tunnel coupling of $2t_{Dq} \approx \hbar f_0 = 7.8$ μeV , which is confirmed by fitting $f_r - f_0$ and κ^* simultaneously with shared parameters to Eqs. (1) and (2) from which we obtain $2t_{Dq} = 7.90 \pm 0.01$ μeV , $g_0/(2\pi) = 51.0 \pm 0.2$ MHz, and $\gamma_{Dq}/(2\pi) = 1.65 \pm 0.01$ GHz. For electrons in silicon, 7.90 μeV is a remarkably large tunnel coupling between states with different S , more than twice the value theoretically estimated in Corna et al.¹³. Overall, we find a substantial

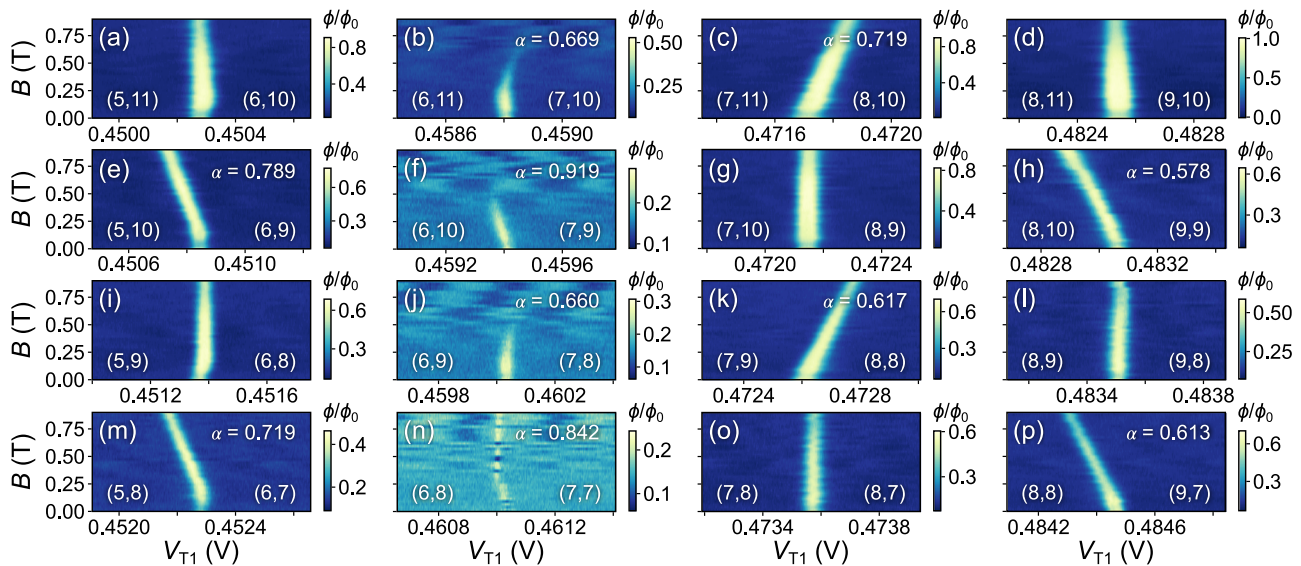


Fig. 3 | Magnetospectroscopy of 16 ICTs. a–p Measurement of the relative phase shift of the 16 ICTs visible in Fig. 1b as a function of B . The numbers in parentheses indicate the electron occupancy of the DQD on either side of the ICT. Energy levels

similar to those of Fig. 2a, b which help explain the magnetospectroscopy are included in “Energy-level diagrams for all 16 ICTs at $B = 0$ T and $B = 0.4$ T”.

asymmetry in the $t_{Dq}(6,9)(7,8)$ and $t_{Dq}(5,10)(6,9)$ tunnel couplings, the first indication of the origin of the non-symmetric PSB.

We further explore the nature of the (5,10)–(6,9) spin-flip transition at $B > 0.3$ T and identify it as an incoherent tunneling process. The large $\gamma_{Dq}/(2\pi) = 1.65 \pm 0.01$ GHz indicates that the system decoheres in the timescale of the resonator excitation and hence, that the measurable signal at the $D_{1/2} - q_{3/2}$ anti-crossing results from incoherent charge transfer. We, therefore, discard coherent tunneling by adiabatic passage as the origin of the signal, despite the large t_{Dq} . Incoherent tunneling may be the consequence of fast state relaxation or pure dephasing. However, at the anti-crossing point, only dephasing in the energy basis can lead to a change in the charge state distribution. Given that coherence is generally dephasing-limited in silicon spin systems, our result aligns with the general observation. The large value of t_{Dq} indicates the presence of significant SOC which may open dephasing channels similar to those observed for charge transitions in corner QDs^{50–52} that are compatible with our measured value of γ_{Dq} . Additionally, spin, valley, and orbital degrees of freedom may all be mixed on a wide energy range by spin-orbit and valley-orbit couplings, which together with Coulomb interactions provide efficient paths for decoherence. In particular, it has been shown in⁵³ that anisotropic QDs such as the ones characterized in this work, are prone to Wigner-like localization: The electrons split apart in the charged dots due to Coulomb repulsion, which results in a significant compression of the energy spectrum³² and mixing of the different degrees of freedom in the presence of spin-orbit and valley-orbit coupling mechanisms^{54–56}. If such localization effects are strong enough, simplified single-particle descriptions like those shown Fig. 2a, b may no longer be valid, even qualitatively. Although the observed γ_{Dq} at the anti-crossing is large, one may expect a reduction away from the anti-crossing where the energy difference of intradot transitions is ϵ -independent, thus encouraging coherent EDSR experiments for electron spins in silicon corner dots away from the anti-crossings followed by readout at said anti-crossing.

Prevalence of Pauli spin blockade lifting

To better understand the prevalence of PSB lifting, we expand the magnetospectroscopy measurements to all 16 ICTs visible in Fig. 1b. The resulting measurements are shown in Fig. 3 in which panels (e) and (j) represent the measurements studied in Fig. 1. The measurements fall into four categories, which are covered in detail in “Energy-level diagrams for all 16 ICTs at $B = 0$ T and $B = 0.4$ T” and summarised here: Most abundant for this DQD is the lack of PSB due to fast spin-flip transitions as seen in Fig. 3c, e, f, h, k, m,

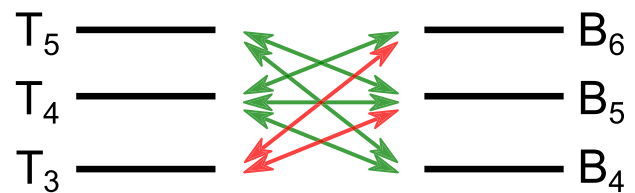


Fig. 4 | Energy level combinations with PSB and PSB lifting. Single-particle energy levels for QD_{T1} and QD_{B1} connected by arrows which show whether the indicated ICT has small or large t_{ij} , red and green arrows respectively. In the case of PSB $\gamma_{ij} < f$ and, in our particular case, PSB lifting is accompanied by $\gamma_{ij} \gtrsim f$. The two (three) lowest energy levels of QD_{T1} (QD_{B1}) are omitted for simplicity.

n, p, among which (f) and (n) are unusual due to the small splitting δ as explained in “Energy-level diagrams for all 16 ICTs at $B = 0$ T and $B = 0.4$ T”. Regular PSB on the other hand is only seen in panels (b) and (j), and partial PSB in which large tunnel couplings relative to δ obscure the blockaded region (see Appendices IV H and IV I) are found in panels (a) and (i). Finally, Fig. 3d, g, l, o show cases in which the spin ground state remains the same for all measured B consistent with previously reported odd-parity transitions⁴⁰. Besides the prevalence, we find that the measurements have a periodicity of two in the QD_{B1} occupancy, indicating broken valley degeneracy and large level separation in QD_{B1} . This agrees with the addition energy that can be inferred from the charge stability diagram and the smaller QD size expected from the lesser channel overlap of G_{B1} . From the sloped magnetospectroscopy measurements in Fig. 3, we extract α and find a consistently large average $\langle \alpha \rangle = 0.7 \pm 0.1$ across the ten ICTs involving different spin manifolds.

By analysis and simulation of each measurement presented in Fig. 3, we construct energy levels similar to those in Fig. 2a, b (see Appendices IV H and IV I), which enable us to understand which combinations of QD energy levels produce fast spin-flipping. The resulting analysis is summarised in Fig. 4, which shows that the transitions that involve the level T_3 have a small tunnel coupling element t_{ij} and low decoherence rate $\gamma_{ij} \ll f$, the latter to avoid tunneling via diabatic passage followed by relaxation (in the charge basis)³³. We hypothesize for the reason of the level-selective and non-symmetric PSB is linked to a recent prediction that, in DQDs subject to strong spin-orbit interactions, PSB may only occur at magnetic field orientations that align with the eigenvectors of the combined g -tensor of the

DQD³⁴, the *magic directions*. Particularly, at these magic directions, the tunnel coupling elements do tend to zero. In our case, for the ICTs in Fig. 3b, j, the g-tensor may have been as such that the external magnetic field may have been favorably aligned resulting in PSB. The dependence of the g-tensor orientation with charge state is backed up by recent experiments described in ref. 57, where a study of the intrinsic spin-orbit fields in InSb DQDs has been performed as a function of charge occupancy, revealing different coupling strengths between different spin branches for different charge configurations.

Discussion

In summary, we have studied the spin-blockade physics of a low-symmetry silicon multi-electron DQD. Through dispersive magnetospectroscopy measurements of 16 ICTs, we found the presence of PSB to be non-symmetric and energy-level selective with a high prevalence of PSB lifting cases. By analyzing the resonator response as a function of DQD detuning and probe frequency using input-output theory, we determined that, in the case where PSB is present, the tunnel coupling element between the spin manifolds involved is small, whereas in the case of PSB lifting, the tunnel coupling was found to be $2t_{Dq} = 7.90 \mu\text{eV}$, the largest reported for electron spins in silicon. Furthermore, we determined that the spin-flip tunneling process is phase-incoherent. Given the low hyperfine fields in silicon⁵⁸, and the observations that spin-orbit coupling is higher in systems with low-symmetry, such as the corner dots studied here¹³, the most likely origin of the large t_{Dq} observed in this study is spin-orbit coupling. The differences in the spin coupling terms for different charge transitions, strongly points towards charge-state-dependent combined DQD g-tensor as the most likely reason³⁴, and encourages angular magnetic field studies of PSB in electron spin systems. Further, the enhanced coupling strength encourages attempts to perform EDSR away from the anti-crossings followed by readout at the chosen anti-crossing. We reason this since, far from the anti-crossing point, the Rabi frequency is proportional to the tunnel coupling term. We also note that the additional signal produced by PSB lifting should provide a way of positively detecting the different states of a spin system, e.g., singlets and triplets, through the selection of appropriate readout detuning values which, through repeated measurements, could enhance the spin readout fidelity. For example, in singlet-triplet qubits, at $g\mu_B B > t_s$ (where t_s is the singlet tunnel coupling), the detuning at which $T_{+(-)}\text{-}S(02)$ anticross could be used to determine a $T_{+(-)}$ outcome and the $S(11)\text{-}S(02)$ anti-crossing point to determine a singlet outcome.

Overall, our results build understanding of PSB physics in silicon important to spin qubit readout, and more particularly to multi-electron QDs system which may become more suitable for scaling due to their capability to better screen potential disorder. Our work further motivates the pursuit of all-electrical control of electron spin qubits although we note that enhance spin-orbit coupling could result in reduced spin coherence^{15,59}.

METHODS

Description of device and measurement setup

Figure 1a depicts the formation of a DQD in a split-gate nanowire field-effect transistor as well as the resonant circuit used to perform dispersive gate-sensing of the DQD. The transistor, which is fabricated on a 300-nm fully-depleted silicon-on-insulator wafer with a buried oxide thickness of 145 nm, consists of a $h = 7$ nm thick, $w = 70$ nm wide silicon nanowire channel, a 6 nm SiO₂ gate oxide, and two TiN/polysilicon gates, G_{B1} and G_{T1} , with 60 nm gate lengths and a $S_g = 40$ nm split-gate separation. We note that G_{T1} overlaps the channel slightly more than G_{B1} due to a 7 ± 3 nm misalignment during fabrication. Spacers made of Si₃N₄ are used to extend the region of intrinsic silicon beneath the gates by 34 nm on either side, thus creating tunnel barriers to the heavily *n*-type-doped source and drain that are held at 0 V. To facilitate gate-based sensing, G_{T1} is wirebonded to a superconducting NbN spiral inductor on a separate chip, thus forming a LC resonant circuit comprised of the capacitance C_d from G_{T1} to ground, parasitic capacitance C_p , and magnetic-field-dependent inductance $L(B)$ of the spiral. At $B = 0$ T, the resonator has a resonance frequency of $f_0(B = 0) = 1.88$ GHz, however, when the magnetic field B is increased, the resonance frequency $f_0(B) = 1/[2\pi\sqrt{L(B)(C_d + C_p)}]$ decreases due to the increasing kinetic inductance of the superconducting spiral inductor³². The inductor, which is fabricated by optical lithography of an 80-nm-thick sputter-deposited NbN film on a sapphire substrate, is situated adjacent to a 50 Ω microstrip waveguide and designed to achieve critical coupling between the resonator and input line. This design results in a large resonator characteristic impedance $Z_r = 560 \Omega$ which, together with the large lever arm $\alpha = C_{T1,T1}/C_{\Sigma T1} - C_{T1,B1}/C_{\Sigma B1} \approx 0.7$ of the wrap-around gates (where C_{ij} is the capacitance between gate i and QD j and $C_{\Sigma i}$ is the total capacitance of QD i), enables a large coherent coupling rate g_0 and thus a large signal-to-noise ratio³⁷. We probe the resonator-DQD system in reflectometry via the microwave transmission line labeled MW_{in} in Fig. 1.

Simulation of device electron density

Figure 5 shows three-dimensional plots of the electronic densities $\rho(\mathbf{r})$ computed in the device for the (5,10), (6,9), and (7,8) QD fillings. The orange charge density isosurfaces enclose 90% of the charge, i.e., 13.5 out of the total $N_T = 15$ electrons. These densities are calculated with a self-consistent Schrödinger-Poisson approximation: the electrons move in the potential created by the gates and by the mean-field density $(N_T - 1)/N_T \times \rho(\mathbf{r})$, where the factor $(N_T - 1)/N_T$ broadly accounts for the fact that each electron only interacts with $N_T - 1$ others in the QDs. Screening in the source and drains is accounted for in a linearized Thomas-Fermi approximation. The simulation methodology gives a reasonable account of the electronic distribution, but does not account for correlation effects (such as the Wigner molecularisation discussed in Sec. II B) that may be significant in corner QDs.

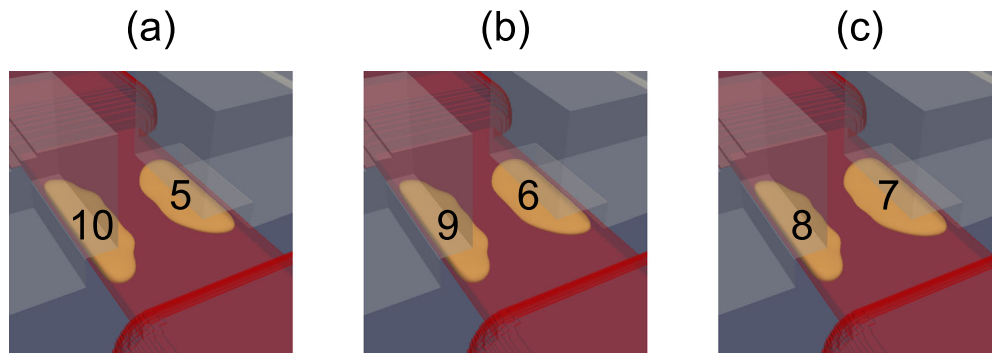


Fig. 5 | Simulation of the electronic density in the device in three electronic configurations totalling 15 electrons. The orange isosurfaces enclose 90% of the electrons. The red regions indicate the silicon nanowire and elevated source and

drain regions. The asymmetrically-placed split gates are represented in gray. Both the gate oxide and the Si₃N₄ spacers have been omitted for clarity. **a, b, c** Show the (5,10), (6,9), and (7,8) charge configurations, respectively.

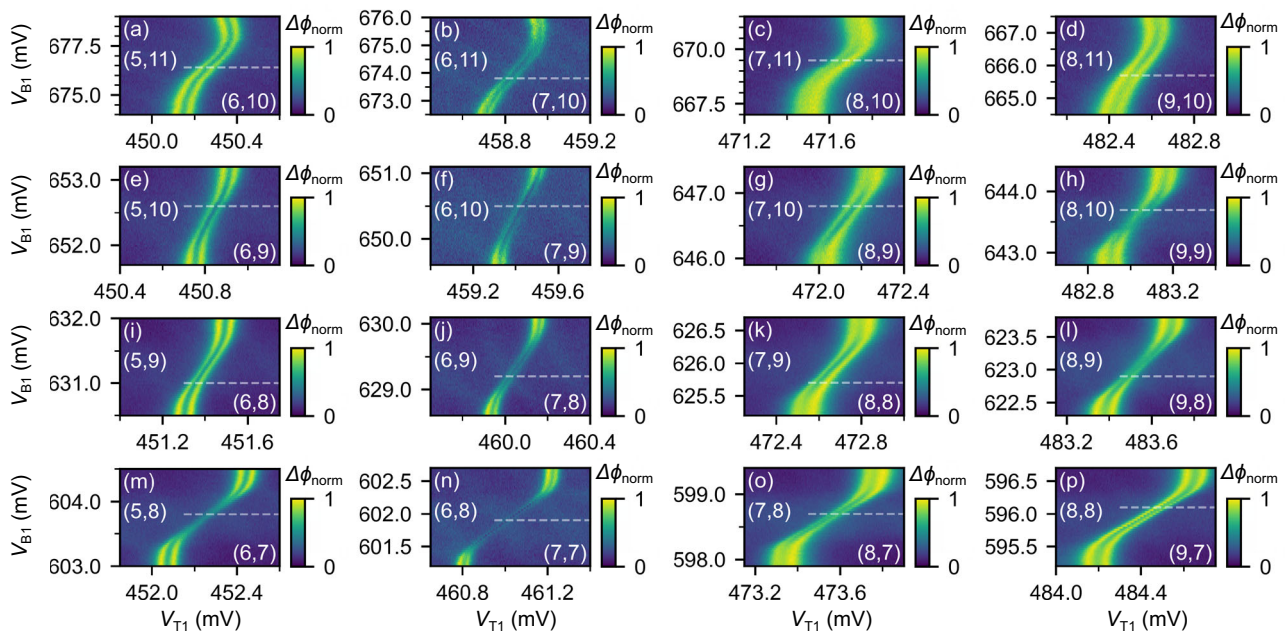


Fig. 6 | Zoomed-in charge stability diagrams of the 16 ICTs in Fig. 1(b). a–p Measurement of the normalized phase shift $\Delta\phi_{\text{norm}}$ of the 16 ICTs visible in Fig. 1b. The numbers in parentheses indicate the electron occupancy of the QDQ on

either side of the ICT and the dashed line indicates the V_{B1} used for the corresponding magnetospectroscopy measurements in Fig. 3. The double peak shape of the lines is a consequence of our choice of measurement frequency f .

Zoomed-in ICT charge stability diagrams

Figure 6 shows zoomed-in charge stability diagrams for each of the 16 ICTs visible in Fig. 1(b) measured at $B = 0$ T. The z-axes for each of the panels of Fig. 6 represents the normalized phase shift $\Delta\phi_{\text{norm}}$ for the measurement in that panel. These charge stability diagrams, which were acquired immediately prior to the magnetospectroscopy measurements in Fig. 3, ensure accurate choice of V_{B1} such that the magnetospectroscopy measurement is done for the positively sloped signal from the ICT and not from a dot-reservoir transition. The V_{B1} used for the magnetospectroscopy measurements is indicated by the dashed lines Fig. 6 (note that the length of the dashed line does not correspond to the V_{T1} range used for magnetospectroscopy). We note that the measurements presented in Figs. 1c, d, 3 and 6 were taken significantly later than the measurement in Fig. 1b during which drifting of the voltages occurred, thereby explaining the slight disagreement in the voltage position of the ICTs between these measurements. Further, the presence of two peaks and one valley in the majority of the ICTs and dot-to-reservoir transitions is associated with our choice of rf probe frequency, $f < f_0$ where f_0 is the natural frequency of the resonator. This choice results in an increase in $\Delta\phi$ whenever the dispersive shift produced by the device reduces the resonance frequency of the resonator f_r such as $f = f_r$ which typically occurs for two values of detuning symmetric with respect to zero either in ICT or dot-to-reservoir transitions. For the experiments in the main text, we select $f \gtrsim f_0$ which avoids the peak doubling effect on the transition lines for all values of B .

Maximum phase shift of (5,10)–(6,9) ICT vs magnetic field

To further characterize the lack of PSB observed for the (5,10)–(6,9) ICT in the magnetospectroscopy measurement of Figs. 1d, 3e, we extract the maximum relative phase shift ϕ_{max}/ϕ_0 , where ϕ_0 is the largest phase shift measured among the 16 ICTs in Fig. 1(b), for each B -field linetrace as seen in Fig. 7. With the exception of a small decrease around $B = 45$ mT, Fig. 7 shows that ϕ_{max}/ϕ_0 remains relatively constant from $B = 0$ to $B = 0.9$. As explained in the main text, the constant phase shift rules out magnetic-field-dependent processes such as standard intradot valley-mediated-relaxation⁶⁰ as the explanation for the lack of PSB. We note that the decreased phase shift around $B = 45$ mT is also observed in magnetospectroscopy measurements

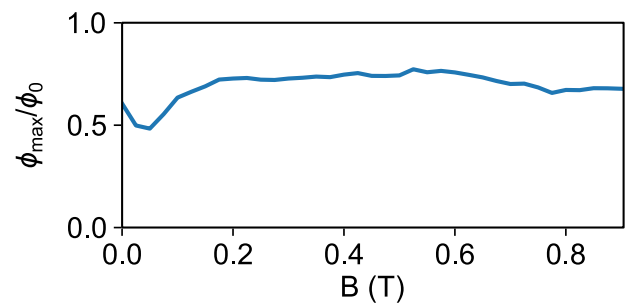


Fig. 7 | Maximum relative phase shift for each B -field linetrace of the magnetospectroscopy measurement presented in Figs. 1d and 3e. The decrease in relative phase shift around $B = 45$ mT is due to a decrease in the resonator Q-factor at this magnetic field.

of all the other ICTs in Fig. 3. We attribute the decrease in phase shift to a reduction of the resonator Q-factor around 45 mT. This deterioration of the Q-factor is also observed in measurements of the reflected spectrum of the resonator as a function of magnetic field during which the device is grounded.

Extracting T_3 – T_4 energy separation

As can be seen from Fig. 2, the D(6,9)–q(6,9) energy separation δ is given by the splitting of levels T_3 and T_4 . The magnitude of δ may be extracted from the magnetospectroscopy measurement presented in Fig. 8 [same data as shown in Figs. 1d, 3e] by extrapolating the sloped signal of the D(5,10)–q(6,9) anti-crossing to $B = 0$ T and determining the voltage separation of the extrapolated signal from the doublet anti-crossing signal at $B = 0$ T. To extrapolate the signal of the D(5,10)–q(6,9) anti-crossing, we extract the center of the phase shift peak for each line trace above $B > 0.2$ T and linearly fit these points to obtain the solid red line in Fig. 8. From the intersection of the linear fit with $B = 0$ T and the central position of the phase shift signal at $B = 0$ T marked with a dotted red line in Fig. 8, we find a voltage separation of $\Delta V = 23.63 \mu\text{V}$, which entails $\delta = \alpha\Delta V = 0.789 \cdot 23.63 \mu\text{V} = 18.65 \mu\text{eV}$.

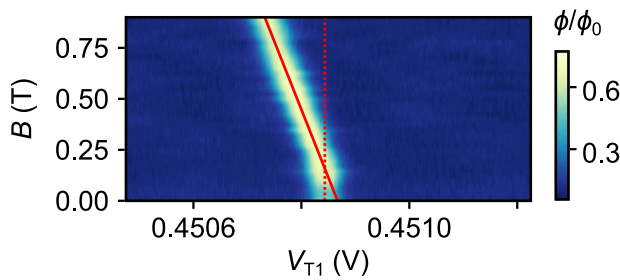


Fig. 8 | Measurement of the relative phase shift of the (5,10)–(6,9) ICT as a function of magnetic field B . The dotted red line marks the central position of the phase shift signal at $B = 0$ T, whereas the solid red line fits the sloped region for $B > 0.2$ T and is extrapolated to $B = 0$ T.

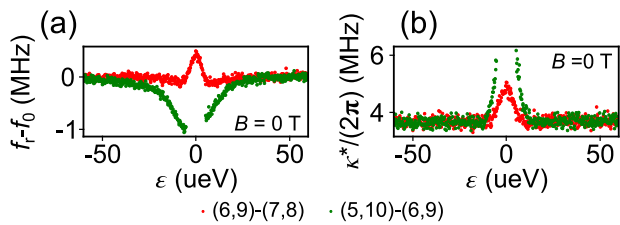


Fig. 9 | Resonator-double quantum dot interaction. **a, b** Resonance frequency f_r and effective linewidth κ^* as a function of ϵ for ICTs (6,9)–(7,8) [red] and (5,10)–(6,9) [green] at $B = 0$ T determined by Lorentzian fits to the data in Fig. 2c, d.

Resonator response for ICTs (6,9)–(7,8) and (5,10)–(6,9) at $B = 0$ T

To emphasize the features of the resonator response at $B = 0$ T shown in Fig. 2c, d, we perform the same analysis and Lorentzian fitting as for Fig. 2e, f and as is described in “Description of fitting procedures”. The f_r and $\kappa^*/(2\pi)$ values obtained for the fits are plotted in Fig. 9. From Fig. 9(a) it is immediately clear that the resonance shifts up [down] for ICT (6,9)–(7,8) [(5,10)–(6,9)], thus providing further evidence for the observations made in the main text that $t_{DD} < hf_0$ and $t_{DD'} > hf_0$. From Fig. 9b, we note a sizeable increase in κ^* around $\epsilon = 0$ indicating a large decoherence rates γ_{DD} and $\gamma_{DD'}$ for the (6,9)–(7,8) and (5,10)–(6,9) doublet transitions. This explains the absence of vacuum Rabi-mode-splitting, which may otherwise have been expected for the resonant regime of ICT (6,9)–(7,8) at $B = 0$ T. The large $\gamma_{DD'}$ also complicates fitting the resonator response of ICT (5,10)–(6,9) around $\epsilon = 0$ to Eq. (3) and is therefore the reason for the lacking data points around $\epsilon = 0$ in Fig. 9. We note that t_{DD} is smaller than t_{Dq} indicating that in this device coupling between states with the same spin angular momentum S can be smaller than between states with different S .

Description of fitting procedures

For the analysis of the resonator response as a function of detuning ϵ , we use the steady-state power reflection coefficient developed from the Heisenberg-Langevin equations of motion in its complex Lorentzian form³⁷

$$|S_{11}| = \left| 1 - \frac{i\kappa_{\text{ext}}/(2\pi)}{f - f_r + \frac{i}{2}\kappa^*/(2\pi)} \right|^2 \quad (3)$$

where $\kappa_{\text{ext}}/(2\pi) = 1.76$ MHz is the external photon decay rate, and where f_r as well as $\kappa^*/(2\pi)$ are defined in Eqs. (1) and (2) in the main text. To obtain the values for f_r and $\kappa^*/(2\pi)$ plotted in Fig. 2g, h as well as Fig. 9a, b below, we fit each ϵ line trace of the data presented in Fig. 2c–f to Eq. (3).

We use the f_r and $\kappa^*/(2\pi)$ data at $B = 0.4$ T plotted in Fig. 2g, h to extract the coherent coupling rate g_0 , tunnel coupling t_{Dq} , and decoherence rate γ_{Dq} . This is done by simultaneously fitting f_r and $\kappa^*/(2\pi)$ to Eqs. (1) and (2) in the main text with shared fitting parameters g_0 , t_{Dq} , and γ_{Dq} and using orthogonal distance regression (ODR) that factors in the errors on both axis for each dataset. The errors given for g_0 , t_{Dq} , and γ_{Dq} in the main text are

obtained from the covariance matrix of the ODR fit and represent one standard deviation.

Energy-level diagrams for all 16 ICTs at $B = 0$ T and $B = 0.4$ T

Figures 10, 11 sketch the single-particle and DQD energy levels as a function of detuning ϵ at $B = 0$ T and $B = 0.4$ T, respectively, for all 16 ICTs visible in the charge stability diagram of Fig. 1b. The single-particle energy levels shown in each panel of Figs. 10, 11 represent the six energy levels shown in Fig. 4, which means that the two (three) lowest and fully-occupied energy levels of QD_{T1} (QD_{B1}) have been omitted for simplicity. The electrons highlighted in red in the single-particle energy diagrams indicate which electrons move QD when crossing an ICT, whereas the presence of a green (red) arrow indicates the presence (lack) of spin-flip tunneling. The color of the DQD energy levels indicate the multiplicity of the multi-particle spin state it represents, and for simplicity, couplings between manifolds of different spin angular momentum are not included in the sketch. To strengthen the link to the main text, the panels of Figs. 10, 11 are organized such that they match the location of the ICTs in the charge stability diagram as well as the panel labels of Fig. 3. This means that one electron is added to QD_{T1} (QD_{B1}) when moving one panel to the right (up). One may note from the first and second column of panels in Figs. 10, 11, that the small splitting δ is a defining feature which, for example, explains the presence of the low-energy quadruplet states.

To assign the spin configurations that model the 16 different magnetospectroscopy maps, we first select the configuration in the single-particle representation of the (5,8)–(6,7) transition [Fig. 10m]. The selection is informed by the charge occupancy and the extracted excited state energy δ yielding a doublet (quadruplet) ground (excited) state. Once this initial spin configuration has been chosen, the rest of the panels follow a natural sequence: the addition of one extra spin in the available state of lowest energy. The only assumption that we make is that the strength of the exchange energy is smaller than the energy level spacing. The assumption results in electron spins pairing up before forming higher spin states at $B = 0$ T. We note that if other initial spin configurations are set for the (5,8)–(6,7) transition or, if we consider the other limit, exchange energy larger than the energy level spacing, the data cannot be reproduced.

In the following, we split the energy diagrams into groups with similar features and use them as a basis for explaining the corresponding magnetospectroscopy panels of Fig. 3:

Panels (c), (e), (f), (h), (k), (m), (n), and (p). As highlighted in the main text and as seen in the case of Fig. 3c, e, f, h, k, m, n, p, the lack of PSB is most abundant among the 16 ICTs. For panels (c), (h), (k), and (p), the phase shift signal of the magnetospectroscopy slopes to one side already from $B > 0$ T. This indicates that the signal at $B = 0$ T arises from the anti-crossing of singlets [see Fig. 10c, (h), (k), and f], but that the singlet tunnel coupling is small such that the signal at $B > 0$ T arises from incoherent tunneling between the singlet and triplet states as indicated by the green arrows in Fig. 11c, h, k, f.

Panels e and (m) are similar to panels (c), (h), (k), and (p), but involve doublet and quadruplet spin states instead of singlets and triplets. Whereas the singlets and triplets were degenerate in one charge configuration at $B = 0$ T, the minimal energy difference between the doublet and quadruplet is given by δ . The signal at $B = 0$ T from the doublet anti-crossing [see Fig. 10e and (m)] therefore persists for longer, and only when $B \gtrsim \delta/(g\mu_B) = 0.16$ T do the quadruplets start to intersect the doublets, resulting in the characteristic sloped signal arising from incoherent tunneling.

Panels (f) and (n) start off similar to panels (c), (h), (k), and (p) with the explanation for what happens in the low-field region of the magnetospectroscopy being the same. However, as seen in Fig. 10f and n, the maximal separation of the triplets from the singlets is δ , which means that the triplets become the ground state for all ϵ when $B \gtrsim 0.16$ T. The straight high-field signal in Fig. 3n may therefore be attributed to the anti-crossing triplet ground state [see Fig. 11n], whereas the lack of any high-field signal in Fig. 3f may be explained by the tunnel coupling of the anti-crossing triplet states

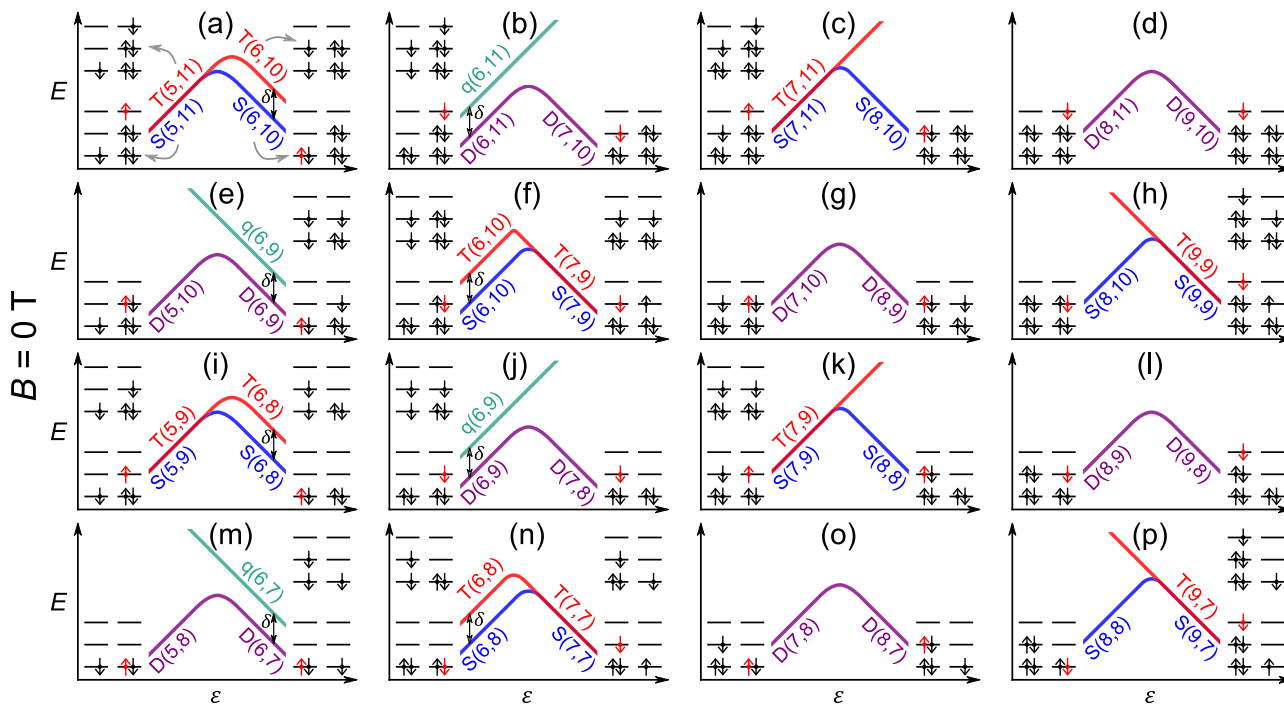


Fig. 10 | Energy spectra at $B = 0$ T. a–p Illustrative single-particle and DQD energy levels as a function of detuning ϵ at $B = 0$ T for the charge states involved in the 16 ICTs present in the charge stability diagram of Fig. 1b. For simplicity, the single-particle energy levels omit the two (three) lowest-lying energy levels of QD_{T1}

(QD_{B1}), such that the six energy levels shown are $T_3, T_4, T_5, B_4, B_5, B_6$ starting from the bottom left. The red electron indicates the electron that moves QD as a function of changes in ϵ .

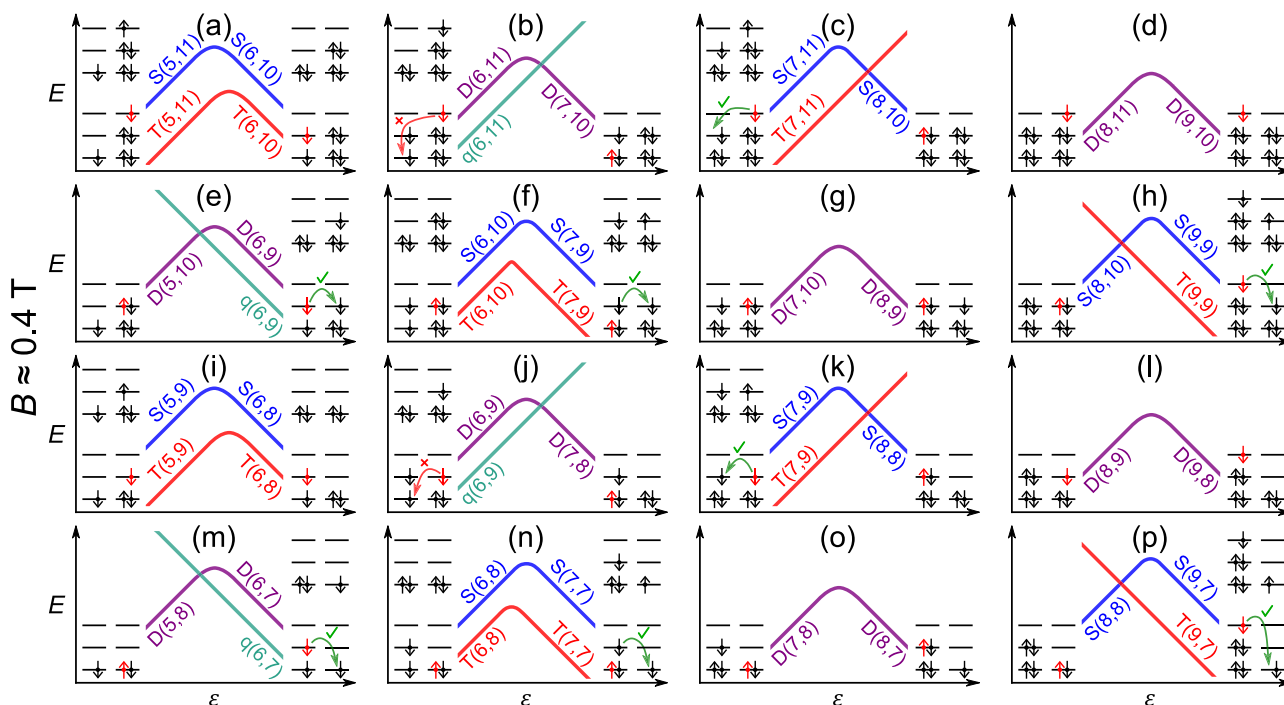


Fig. 11 | Energy spectra at $B = 0.4$ T. a–p Illustrative single-particle and DQD energy levels as a function of detuning ϵ at $B = 0.4$ T for the charge states involved in the 16 ICTs present in the charge stability diagram of Fig. 1b. For simplicity, the single-particle energy levels omit the two (three) lowest-lying energy levels of QD_{T1} (QD_{B1}), such that the six energy levels shown are $T_3, T_4, T_5, B_4, B_5, B_6$ starting from

the bottom left. The red electron indicates the electron that moves QD as a function of changes in detuning, and the green (red) arrows indicate (the lack of) spin-flip tunneling. Note that the green arrows in (f, n) indicate spin-flip tunneling in the singlet–triplet manifold, which happens only when $B \lesssim \delta/(g\mu_B) = 0.16$ T.

Table 1 | Parameters used to perform qualitative magnetospectroscopy simulations shown in Fig. 12 for the energy levels shown in Figs. 10 and 11

Panel	$2t_S$ or $2t_D$ (μeV)	$2t_T$ or $2t_Q$ (μeV)	δ_N (μeV)	δ_P (μeV)	Relaxation regime
a	20	20	0	18	Slow
b	15	20	18	>120	Slow
c	10	20	0	>120	Fast
d	20	20	>120	>120	Fast
e	20	20	>120	18	Fast
f	10	3	18	0	Fast
g	20	20	>120	>120	Fast
h	10	20	>120	0	Fast
i	20	20	0	18	Slow
j	7	20	18	>120	Slow
k	10	20	0	>120	Fast
l	20	20	>120	>120	Fast
m	20	20	>120	18	Fast
n	10	20	18	0	Fast
o	20	20	>120	>120	Fast
p	10	20	>120	0	Fast

Columns two through five list the magnitude of the needed energy spectrum parameters, and the last column indicates whether the simulations consider the slow or fast relaxation regime. All simulations use $T = 80$ mK.

being so small that the resonator probe drives diabatic Landau-Zener transitions across the anti-crossing⁶¹.

Panels (b) and (j). Cases of clear PSB are found in panels (b) and (j), which involve doublet and quadruplet states, and whose magnetospectroscopy matches previous observations of dispersively-detected PSB^{24,40–43}. Similar to panels (e) and (m), the low-field signal arises from the doublet anti-crossing [see Fig. 10b, j]. In this case however, when $B \gtrsim 0.16$ T, PSB begin to manifest because spin-flip tunneling is prohibited for energy level transitions T_3 – B_5 and T_3 – B_6 as shown with the red arrows in Fig. 11b, j.

Panels (a) and (i). Panels (a) and (i) bear similarities with panels (f) and (n) because the triplet anti-crossing also here becomes the ground state already when $B \gtrsim 0.16$ T, giving rise to the high-field signal [see Fig. 11a, i]. At low fields, $B < 0.16$ T, the signal comes primarily from the singlet anti-crossing. According to our model, PSB is expected from the energy level transitions T_3 – B_5 and T_3 – B_6 . However, in our experiment, the tunnel coupling of both the singlet and triplet manifolds is large compared to δ for panels (a) and (i) [this is the condition for which the PSB readout window is rendered inefficient], and hence the singlet and triplet signal regions overlap where PSB should have been observed²⁴. We therefore classify these two panels as cases of partial PSB.

Panels (d), (g), (l), and (o). Finally, panels (d), (g), (l), and (o) represent simple cases of odd-parity transitions⁴⁰ where the anti-crossing of just one spin manifold, the doublet, is the ground state for the entire range of magnetic fields studied. The lack of any higher spin manifolds indicates that the energy level separation between levels T_4 and T_5 as well as the separation between levels in QD_{B1} greater than $g\mu_B \cdot 0.9$ T ≈ 100 μeV , i.e., substantially larger than δ .

Magnetospectroscopy simulations for all 16 ICTs

To support the explanations of the observed magnetospectroscopy provided in “Energy-level diagrams for all 16 ICTs at $B = 0$ T and $B = 0.4$ T”, we

qualitatively simulate the resonator response as a function of magnetic field for the energy spectra in Figs. 10, 11. We use the semi-classical approximation³³ where the effect of the quantum system on a classical resonator is expressed in terms of the parametric capacitance

$$C_{\text{pm}} = (e\alpha)^2 \frac{\partial \langle n_2 \rangle}{\partial \epsilon} \quad (4)$$

where e is the electron charge, α is the interdot lever arm, $\langle n_2 \rangle$ is the occupation probability of the QD connected to the resonator. We further consider the small signal regime where the phase response of the resonator is directly proportional to the change in parametric capacitance, $\phi \propto \Delta C_{\text{pm}}$. The QD occupation probability can be expanded in terms of the polarization and occupation probabilities of each individual eigenstate, $\langle n_2 \rangle_i$ and P_i respectively

$$\langle n_2 \rangle = \sum_i \langle n_2 \rangle_i P_i \quad (5)$$

In this case, the parametric capacitance can be expanded in terms of its two principal constituents, the quantum capacitance and tunneling capacitance^{33,62}:

$$C_{\text{pm}} = (e\alpha)^2 \underbrace{\sum_i \frac{\partial \langle n_2 \rangle_i}{\partial \epsilon} P_i}_{\text{quantum}} + \underbrace{\langle n_2 \rangle_i \frac{\partial P_i}{\partial \epsilon}}_{\text{tunneling}} \quad (6)$$

Finally, to perform the simulations we consider the general expression of the polarizations:

$$\langle n_2 \rangle_i = \frac{1}{2} \left(1 + 2 \frac{\partial E_i}{\partial \epsilon} \right) \quad (7)$$

To produce the simulations, the parameters that are needed are the couplings between eigenenergies in the same spin branch t_p , the energy splittings at large absolute detuning δ_i and the temperature T . In each panel, we either use the slow relaxation regime, where only quantum capacitance manifests, or the fast relaxation regime, where both quantum and tunneling capacitance contribute to the total parametric capacitance³³. The latter implies that we are simulating fast decoherence via relaxation and hence we use the thermal probabilities $P_i = P_i^{\text{th}}$. Table 1 summarises the parameters used to simulate each of the 16 energy spectra. Columns two and three list the tunnel couplings in μeV between the spin manifolds present in the energy spectrum at the given charge occupation (see “Energy-level diagrams for all 16 ICTs at $B = 0$ T and $B = 0.4$ T”), whereas columns four and five list the energy splittings in μeV at large negative (positive) detuning δ_N (δ_P). Note that values of $\delta_N = \delta_P > 120$ μeV simply indicate that the splitting is larger than 120 μeV and hence renders the high-spin anti-crossing unobservable within the measured and simulated range of magnetic fields. Finally, the last column denotes the relaxation regime simulated, i.e., whether tunneling capacitance is included or not. We use a temperature of $T = 80$ mK for all simulations and $\delta_{N(P)} = 18$ μeV for all splittings that correspond to the T_3 – T_4 separation δ .

Based on the proportionality $\phi \propto \Delta C_{\text{pm}}$, we use Eqs. (6) and (7) and the parameters in Table 1 to qualitatively simulate the normalized phase shift ϕ_{norm} and magnetospectra for the energy spectra sketched in Figs. 10, 11. The simulation results are shown in Fig. 12. For the simulation of Fig. 12f, we introduce a suppression of the phase shift signal for $B > 0.2$ T to account for Landau-Zener transitions which cause the change in QD occupation probability to approach zero. Overall, the simulations represent the measured magnetospectra in Fig. 3 well.

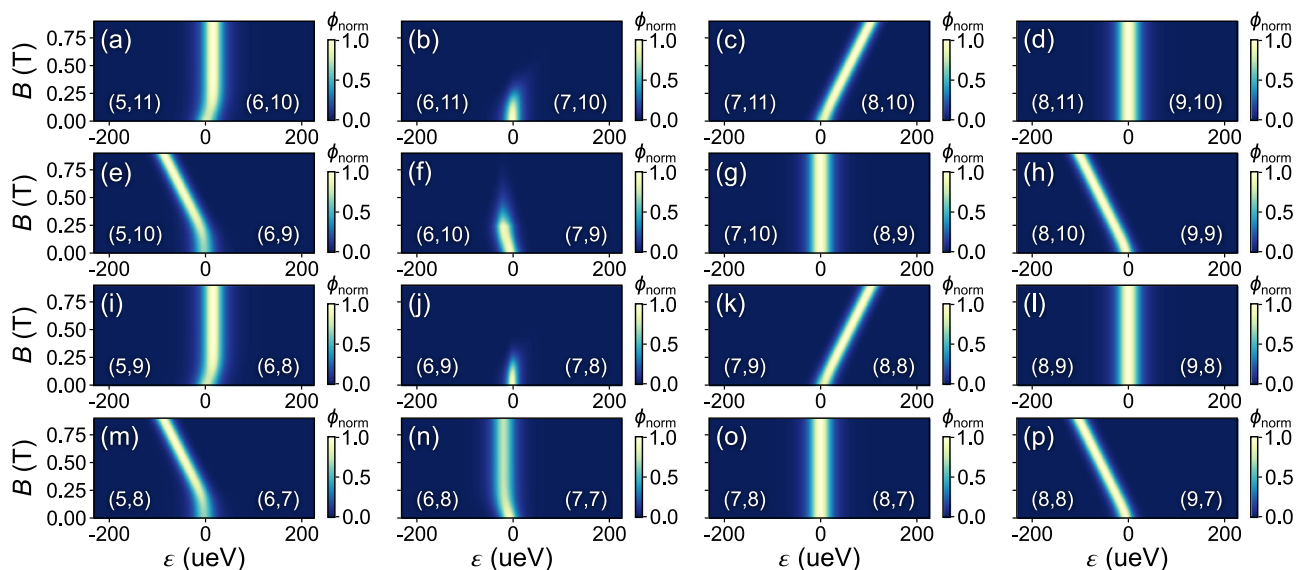


Fig. 12 | Magnetospectroscopy simulations of the 16 studied ICTs. a–p Qualitative simulation of the normalized phase shift of each ICT visible in Fig. 1b and their energy spectra in Figs. 10, 11 as a function of B using the parameters in Table 1. The numbers in parentheses indicate the electron occupancy of the DQD on either side of the ICT.

Data availability

The data that support the findings of this study are available from the corresponding author on a reasonable request.

Code availability

The code developed to simulate the magnetospectroscopy data is available from the corresponding author on a reasonable request.

Received: 3 January 2023; Accepted: 12 February 2024;

Published online: 06 March 2024

References

- Loss, D. & DiVincenzo, D. P. Quantum computation with quantum dots. *Phys. Rev. A* **57**, 120 (1998).
- Veldhorst, M. et al. An addressable quantum dot qubit with fault-tolerant control-fidelity. *Nat. Nanotechnol.* **9**, 981 (2014).
- Yang, C. H. et al. Silicon qubit fidelities approaching incoherent noise limits via pulse engineering. *Nat. Electron.* **2**, 151 (2019).
- Petit, L. et al. Universal quantum logic in hot silicon qubits. *Nature* **580**, 355 (2020).
- Yang, C. H. et al. Operation of a silicon quantum processor unit cell above one kelvin. *Nature* **580**, 350 (2020).
- Camenzind, L. C. et al. A hole spin qubit in a fin field-effect transistor above 4 Kelvin. *Nat. Electron.* **5**, 178 (2022).
- Maurand, R. et al. A CMOS silicon spin qubit. *Nat. Commun.* **7**, 13575 (2016).
- Pauka, S. J. et al. A cryogenic cmos chip for generating control signals for multiple qubits. *Nat. Electron.* **4**, 64 (2021).
- Zwerver, A. M. J. et al. Qubits made by advanced semiconductor manufacturing. *Nat. Electron.* **5**, 184 (2021).
- Li, R. et al. A flexible 300 mm integrated Si MOS platform for electron- and hole-spin qubits exploration. In *Proc. IEEE International Electron Devices Meeting (IEDM)* 33–38 (IEEE, 2020).
- Xue, X. et al. CMOS-based cryogenic control of silicon quantum circuits. *Nature* **593**, 205 (2021).
- Huang, W., Veldhorst, M., Zimmerman, N. M., Dzurak, A. S. & Culcer, D. Electrically driven spin qubit based on valley mixing. *Phys. Rev. B* **95**, 075403 (2017).
- Corna, A. et al. Electrically driven electron spin resonance mediated by spin-valley-orbit coupling in a silicon quantum dot. *npj Quantum Inf.* **4**, 6 (2018).
- Vahapoglu, E. et al. Coherent control of electron spin qubits in silicon using a global field. *npj Quantum Inf.* **8**, 126 (2022).
- Piot, N. et al. A single hole spin with enhanced coherence in natural silicon. *Nat. Nanotech.* **17**, 1072 (2022).
- Ahmed, I. et al. Radio-frequency capacitive gate-based sensing. *Phys. Rev. Appl.* **10**, 014018 (2018).
- Pakkiam, P. et al. Single-shot single-gate rf spin readout in silicon. *Phys. Rev. X* **8**, 041032 (2018).
- West, A. et al. Gate-based single-shot readout of spins in silicon. *Nat. Nanotechnol.* **14**, 437 (2019).
- Crippa, A. et al. Gate-reflectometry dispersive readout and coherent control of a spin qubit in silicon. *Nat. Commun.* **10**, 2776 (2019).
- Elzerman, J. M. et al. Single-shot read-out of an individual electron spin in a quantum dot. *Nature* **430**, 431 (2004).
- Ono, K., Austing, D. G., Tokura, Y. & Tarucha, S. Current rectification by Pauli exclusion in a weakly coupled double quantum dot system. *Science* **297**, 1313 (2002).
- Schoelkopf, R. J., Wahlgren, P., Kozhevnikov, A. A., Delsing, P. & Prober, D. E. The radio-frequency single-electron transistor (RFSET): a fast and ultrasensitive electrometer. *Science* **280**, 1238 (1998).
- Ciriano-Tejel, V. N. et al. Spin readout of a CMOS quantum dot by gate reflectometry and spin-dependent tunneling. *PRX Quantum* **2**, 010353 (2021).
- Betz, A. C. et al. Dispersively detected Pauli spin-blockade in a silicon nanowire field-effect transistor. *Nano Lett.* **15**, 4622 (2015).
- Zheng, G. et al. Rapid gate-based spin read-out in silicon using an on-chip resonator. *Nat. Nanotechnol.* **14**, 742 (2019).
- Fogarty, M. A. et al. Integrated silicon qubit platform with single-spin addressability, exchange control and single-shot singlet-triplet readout. *Nat. Commun.* **9**, 4370 (2018).
- Harvey-Collard, P. et al. High-fidelity single-shot readout for a spin qubit via an enhanced latching mechanism. *Phys. Rev. X* **8**, 021046 (2018).
- Zhao, R. et al. Single-spin qubits in isotopically enriched silicon at low magnetic field. *Nat. Commun.* **10**, 5500 (2019).
- Seedhouse, A. E. et al. Pauli blockade in silicon quantum dots with spin-orbit control. *PRX Quantum* **2**, 010303 (2021).
- Fujita, T. et al. Signatures of hyperfine, spin-orbit, and decoherence effects in a Pauli spin blockade. *Phys. Rev. Lett.* **117**, 206802 (2016).

31. van der Heijden, J. et al. Readout and control of the spin-orbit states of two coupled acceptor atoms in a silicon transistor. *Sci. Adv.* **4**, eaat9199 (2018).
32. Lundberg, T. et al. Spin quintet in a silicon double quantum dot: spin blockade and relaxation. *Phys. Rev. X* **10**, 041010 (2020).
33. Mizuta, R., Otxoa, R. M., Betz, A. C. & Gonzalez-Zalba, M. F. Quantum and tunneling capacitance in charge and spin qubits. *Phys. Rev. B* **95**, 045414 (2017).
34. Sen, A., Frank, G., Kolok, B., Danon, J. & Pályi, A. Classification and magic magnetic-field directions for spin-orbit-coupled double quantum dots. *Phys. Rev. B* **108**, 245406 (2023).
35. Leon, R. C. C. et al. Coherent spin control of s-, p-, d- and f-electrons in a silicon quantum dot. *Nat. Commun.* **11**, 797 (2020).
36. Leon, R. C. C. et al. Bell-state tomography in a silicon many-electron artificial molecule. *Nat. Commun.* **12**, 3228 (2021).
37. Ibberson, D. J. et al. Large dispersive interaction between a CMOS double quantum dot and microwave photons. *PRX Quantum* **2**, 020315 (2021).
38. Gilbert, W. et al. Single-electron operation of a silicon-cmos 2 × 2 quantum dot array with integrated charge sensing. *Nano Lett.* **20**, 7882 (2020).
39. House, M. G. et al. Radio frequency measurements of tunnel couplings and singlet-triplet spin states in Si:P quantum dots. *Nat. Commun.* **6**, 8848 (2015).
40. Schroer, M. D., Jung, M., Petersson, K. D. & Petta, J. R. Radio frequency charge parity meter. *Phys. Rev. Lett.* **109**, 166804 (2012).
41. Urdampilleta, M. et al. Charge dynamics and spin blockade in a hybrid double quantum dot in silicon. *Phys. Rev. X* **5**, 031024 (2015).
42. Landig, A. J. et al. Microwave-cavity-detected spin blockade in a few-electron double quantum dot. *Phys. Rev. Lett.* **122**, 213601 (2019).
43. Hutin, L. et al. Gate reflectometry for probing charge and spin states in linear Si MOS split-gate arrays. In *Proc. IEEE International Electron Devices Meeting (IEDM) 37.7.1–37.7.4* (IEEE, 2019).
44. Johnson, A. C., Petta, J. R., Marcus, C. M., Hanson, M. P. & Gossard, A. C. Singlet-triplet spin blockade and charge sensing in a few-electron double quantum dot. *Phys. Rev. B* **72**, 165308 (2005).
45. Kouwenhoven, L. P., Austing, D. G. & Tarucha, S. Few-electron quantum dots. *Rep. Prog. Phys.* **64**, 701 (2001).
46. Petersson, K. D. et al. Circuit quantum electrodynamics with a spin qubit. *Nature* **490**, 380 (2012).
47. Blais, A., Grimsmo, A. L., Girvin, S. M. & Wallraff, A. Circuit quantum electrodynamics. *Rev. Mod. Phys.* **93**, 025005 (2021).
48. Childress, L., Sørensen, A. S. & Lukin, M. D. Mesoscopic cavity quantum electrodynamics with quantum dots. *Phys. Rev. A* **69**, 042302 (2004).
49. Koch, J. et al. Charge-insensitive qubit design derived from the Cooper pair box. *Phys. Rev. A* **76**, 042319 (2007).
50. Dupont-Ferrier, E. et al. Coherent coupling of two dopants in a silicon nanowire probed by Landau-Zener-Stückelberg interferometry. *Phys. Rev. Lett.* **110**, 136802 (2013).
51. Gonzalez-Zalba, M. F. et al. Gate-sensing coherent charge oscillations in a silicon field-effect transistor. *Nano Lett.* **16**, 1614 (2016).
52. Chatterjee, A. et al. A silicon-based single-electron interferometer coupled to a fermionic sea. *Phys. Rev. B* **97**, 045405 (2018).
53. Abadillo-Uriel, J. C., Martinez, B., Filippone, M. & Niquet, Y.-M. Wigner molecularization in asymmetric quantum dots. *Phys. Rev. B* **104**, 195305 (2021).
54. Ercan, H. E., Coppersmith, S. N. & Friesen, M. Strong electron-electron interactions in Si/SiGe quantum dots. *Phys. Rev. B* **104**, 235302 (2021).
55. Ercan, H. E., Friesen, M. & Coppersmith, S. N. Charge-noise resilience of two-electron quantum dots in Si/SiGe heterostructures. *Phys. Rev. Lett.* **128**, 247701 (2022).
56. Corrigan, J. et al. Coherent control and spectroscopy of a semiconductor quantum dot Wigner molecule. *Phys. Rev. Lett.* **127**, 127701 (2021).
57. Han, L. et al. Variable and orbital-dependent spin-orbit field orientations in a insb double quantum dot characterized via dispersive gate sensing. *Phys. Rev. Appl.* **19**, 014063 (2023).
58. Prance, J. R. et al. Single-shot measurement of triplet-singlet relaxation in a Si/SiGe double quantum dot. *Phys. Rev. Lett.* **108**, 046808 (2012).
59. Gilbert, W. et al. On-demand electrical control of spin qubits. *Nat Nanotech* **18**, 131 (2023).
60. Yang, C. H. et al. Spin-valley lifetimes in a silicon quantum dot with tunable valley splitting. *Nat. Commun.* **4**, 2069 (2013).
61. Nielsen, E., Barnes, E., Kestner, J. P. & Das Sarma, S. Six-electron semiconductor double quantum dot qubits. *Phys. Rev. B* **88**, 195131 (2013).
62. Esterli, M., Otxoa, R. M. & Gonzalez-Zalba, M. F. Small-signal equivalent circuit for double quantum dots at low-frequencies. *Appl. Phys. Lett.* **114**, 253505 (2019).

Acknowledgements

We thank M. Benito and C. Lainé for valuable discussions. This research has received funding from the European Union's Horizon 2020 Research and Innovation Programme under grant agreements No 688539 and 951852. T.L. acknowledges support from the EPSRC Cambridge NanoDTC, EP/L015978/1. D.J.I. is supported by the Bristol Quantum Engineering Centre for Doctoral Training, EPSRC Grant No. EP/L015730/1. M.F.G.-Z. acknowledges support from UKRI Future Leaders Fellowship [grant number MR/V023284/1]. C.L. and J.W.A.R. acknowledge the EPSRC through the Core-to-Core International Network "Oxide Super-spin" (EP/P026311/1) and the "Superconducting Spintronics" Programme Grant (EP/N017242/1).

Author contributions

T.L. and M.F.G.-Z. acquired the data. J.L., J.C.A.-U., M.F., and Y.-M.N. developed the single-particle energy level modeling. L.H., B.B., and M.V. designed and fabricated the samples. A.N. and M.F.G.-Z. developed the CirQED modeling. C.-H.L., N.S., and J.W.A.R. deposited the NbN films. L.I. and D.J.I. fabricated the resonators. T.L. and M.F.G.-Z. performed the quantum capacitance simulations. Y.-M.N. and M.F.G.-Z. supervised the project. T.L. and M.F.G.-Z. wrote the manuscript with input from all co-authors.

Competing interests

M.F.G.-Z. is employed by Quantum Motion Technologies, a start-up focusing on building a silicon-based quantum computer. The rest of the authors declare that they have no competing interests.

Additional information

Correspondence and requests for materials should be addressed to M. Fernando Gonzalez-Zalba.

Reprints and permissions information is available at <http://www.nature.com/reprints>

Publisher's note Springer Nature remains neutral with regard to jurisdictional claims in published maps and institutional affiliations.

Open Access This article is licensed under a Creative Commons Attribution 4.0 International License, which permits use, sharing, adaptation, distribution and reproduction in any medium or format, as long as you give appropriate credit to the original author(s) and the source, provide a link to the Creative Commons licence, and indicate if changes were made. The images or other third party material in this article are included in the article's Creative Commons licence, unless indicated otherwise in a credit line to the material. If material is not included in the article's Creative Commons licence and your intended use is not permitted by statutory regulation or exceeds the permitted use, you will need to obtain permission directly from the copyright holder. To view a copy of this licence, visit <http://creativecommons.org/licenses/by/4.0/>.

© The Author(s) 2024